

Porous graphene-assisted dynamic Pd catalysis for superior hydrogenation

Jie Gao^{a,b}, Chao Jia^{a,b}, Fengbo Yu^{a,b}, Yang Cao^c, Linyu Zhu^d, Aodi Li^{a,b}, Liming Sun^{a,b}, Litao Lin^{a,b}, Xuan Wu^{a,b}, Zhelin He^{a,b}, Zhongyue Zhou^d, James H. Clark^{a,b,e}, Lina Li^f, Yong Wang^g, Xiangdong Zhu^{a,*}, Shicheng Zhang^{a,b,**}

^a Shanghai Technical Service Platform for Pollution Control and Resource Utilization of Organic Wastes, Shanghai Key Laboratory of Atmospheric Particle Pollution and Prevention (LAP3), Department of Environmental Science and Engineering, Fudan University, Shanghai 200438, China

^b Shanghai Institute of Pollution Control and Ecological Security, Shanghai 200092, China

^c Department of Civil and Environmental Engineering, The Hong Kong Polytechnic University, the Hong Kong Special Administrative Region of China

^d School of Mechanical Engineering, Shanghai Jiao Tong University, Shanghai 200240, China

^e Green Chemistry Centre of Excellence, Department of Chemistry, University of York, York YO10 5DD, UK

^f Shanghai Synchrotron Radiation Facility, Shanghai Advanced Research Institute, Shanghai, 201204, China

^g Advanced Materials and Catalysis Group, Institute of Catalysis, Department of Chemistry, Hangzhou 310028, China



ARTICLE INFO

Keywords:
Porous graphene
Hydrogenation
The All-in-one system
Dynamic Pd catalysis

ABSTRACT

Statically immobilized Pd active sites leads to suboptimal hydrogenation efficacy even under harsh reaction conditions, and dynamic catalysis for individual requirements of H₂ dissociation and substrate activation is devoid. Here, we have developed an innovative *All-in-one* system that employs dynamic Pd catalysis assisted by porous graphene, enabling hydrogenation to be conducted under mild conditions. The conversion of vanillin at 30 °C is 99% and the yield of 2-methoxy-4-methylphenol is >95%, significantly exceeding the reported records. The uniformly distributed N-doping and thin sheets of porous graphene induce Pd single-atom (PdN₄) formation, and inhibit rapid agglomeration to nanoparticles (Pd NPs) for assisting dynamic catalysis. High-pressure process analysis and theoretical calculations reveal that excellent activity comes from the synergistic effects of PdN₄ and Pd NPs. Importantly, *All-in-one* system is applicable for complex bio-oil hydrogenation and for a broad spectrum of unsaturated substrates.

1. Introduction

Palladium (Pd) hydrogenation of unsaturated substrates constitutes a highly important process in chemical manufacturing, as the products are crucial intermediates for many sectors including pharmaceuticals, fragrances, fuels and increasingly in biorefineries [1–4]. In the hydrogenation reaction, the substrate is activated and then converted by active hydrogen (H[•]) generated from H₂ dissociation [5–8]. It has been well demonstrated that Pd single atom (Pd₁) can effectively promote substrate activation, while Pd nanoparticles (NPs) contribute more to H₂ dissociation [9–11]. Therefore, hydrogenation kinetics rely crucially on the synergistic function between Pd₁ and Pd NPs. Based on this, a series of catalysts comprising both Pd₁ and Pd NPs has been previously reported to boost hydrogenation reaction [9,12]. However, statically immobilized Pd NPs cannot satisfy the individual requirements of H₂

dissociation and substrate activation. Moreover, the atomic efficiency was restricted due to the constrained accessibility between the substrate and the Pd inside the particle [13–15]. Therefore, there is an urgency to design a catalysis that matches each reaction step with its privileged active sites and maintains high atomic efficiency.

To fulfill the above requirements, it has been disclosed to combine active site generation and substrate conversion for enhanced catalytic activity and high atomic efficiency [16–18]. Considering that Pd NPs are generated through the growth and aggregation of Pd₁, the agglomeration of Pd₁ leads to the increased Pd NPs, which align with the requirements for substrate activation and H₂ dissociation during hydrogenation. Based on this, we hypothesized that it would be feasible to combine dynamic Pd reduction process with the substrate conversion process for optimum hydrogenation activity and high atomic efficiency [19,20].

* Corresponding author.

** Corresponding author at: Shanghai Technical Service Platform for Pollution Control and Resource Utilization of Organic Wastes, Shanghai Key Laboratory of Atmospheric Particle Pollution and Prevention (LAP3), Department of Environmental Science and Engineering, Fudan University, Shanghai 200438, China.

E-mail addresses: zxdjewett@fudan.edu.cn (X. Zhu), zhangsc@fudan.edu.cn (S. Zhang).

Inspired by the aforementioned hypothesis, we envisioned a strategy of “dynamic Pd catalysis” to combine anchoring and *in-situ* reduction of Pd on porous graphene with synchronous conversion of substrate (Fig. 1a). It is undeniable that graphene as a catalyst or catalyst support consists of adjustable physical and chemical properties [21]. Various researches have been undertaken to promote its activity and enhance its stability through chemical modification methods, including element doping, defect introduction, and surface modification [22–25]. It has been documented that thin sheets graphene structure with a uniform N distribution can offer sufficient sites for metal anchoring and stabilization when used as a support [26–29]. Moreover, the formation of metal–N coordination structure can effectively prevent swift metal aggregation [30,31]. Therefore, porous graphene with N-doping is promising for maintaining the co-existence of Pd_1 and Pd NPs and, consequently, realizing their synergistic effect. However, different from the traditional static two-step system (catalyst reduction followed by application), a dynamic reaction system was proposed to achieve high atomic efficiency. Denoted as *All-in-one* system, it integrates the Pd anchoring and *in-situ* reduction, and synchronous substrate conversion.

Herein, we design an *All-in-one* system that utilizes porous graphene as a support material for achieving a highly effective Pd catalysis in the dynamic hydrogenation of unsaturated substrates. The porous graphene allows for the uniform anchoring of Pd^{2+} ions, which are then rapidly reduced to Pd_1 and slowly aggregated into Pd NPs, facilitating the dynamic catalysis. The synergistic effects of Pd_1 and Pd NPs on each step of the hydrogenation reaction were revealed through process analysis and theoretical calculations. Furthermore, its broad-spectrum application potential were studied using multiple unsaturated substrates containing C=C, C=O, and $-NO_2$ groups. The results of this study demonstrate the versatility and effectiveness of our *All-in-one* system, highlighting its potential for various applications in the field of catalysis.

2. Experimental

2.1. Manufacturing of porous graphene as carbon support for the *All-in-one* system

In order to obtain high catalytic activity, porous graphene for Pd anchoring was synthesized via flash Joule heating reaction of porous biochar [32]. Briefly, porous biochar was placed in a quartz tube that was compacted with two copper electrodes at each end for low resistivity and then powered a triple pulse voltage (150 V) with 50 ms in a vacuum desiccator (0.6 psi) (Fig. S1). The millisecond ultra-high temperature (up to 3000 °C) in flash Joule heating reaction induced the

graphitization of carbon sketelon, and simultaneous electrical exfoliation function promoted the formation of porous graphene (Fig. S2). Besides, the porosity of porous graphene was due to the retention of its precursor. In order to distinguish the effect of low-density heteroatom resulted by large specific areas and thin sheets structure in porous graphene, biochar lacking both N element and sheets structure, graphene devoid of sheets structure, and porous biochar missing N element were synthesized and tested, respectively. Detailed information can be found in Supporting Information (Section 1.1 and 1.2).

2.2. Integrated Pd reduction and substrate hydrogenation in the *All-in-one* system

To integrated Pd reduction and substrate activation, $PdCl_2$ (2.5 wt %), the substrate (2 mmol), and isopropanol (20 mL) as solvent were stirred together in a 50 mL stainless steel batch reactor (MC50, Senlon) at 30 °C under 700 rpm. To well confine Pd NPs, porous graphene (30 mg) was employed as support in the *All-in-one* system. Then, 0.5 MPa H_2 was pressurized into the reactor to activate the reduction of Pd^{2+} . Then, dissociation of H_2 and hydrogenation of vanillin (VAN) occurred simultaneously during the dynamic process described above. To compare the advantage of dynamic Pd catalysis, the activity of conventional static catalysis was also measured (Fig. S3). The details are presented in the Supporting Information (Section 1.3).

To monitor the mass changes of reactant and its products during the reaction, 15 μ L samples were taken *in-situ* from the *All-in-one* system every 3 min under the reaction pressure by using capillary sampling with a ferrule (0.4 mmVG cond) to prevent air leakage [33]. Briefly, a fused silica capillary tube with a length of 200 mm and an inner diameter of 50 μ m was directly mounted to the bottom of the reactor. When the reactor was sealed and heated, the liquid sample was forced through the capillary forced by the internal pressure. Due to the negligible pressure and sample losses per sampling, this high-pressure process analysis facilitated the understanding of VAN conversion and MMP production without disrupting the reaction system. To determine the concentrations of the substrates, 200 mg/L DL-menthol was assed to each sample as an internal standard. All the experiments were conducted in triplicate, and all samples was analyzed using gas chromatography mass spectrometry (GC-MS). The details can be found in Supplementary Information (Section 1.4).

The conversion of VAN and the selectivity and yield of products were calculated using the following equations:

$$\text{Conversion}(\%) = (1 - \frac{\text{Wfeedstock after reaction}}{\text{Wfeedstock}}) \times 100\% \quad (1)$$

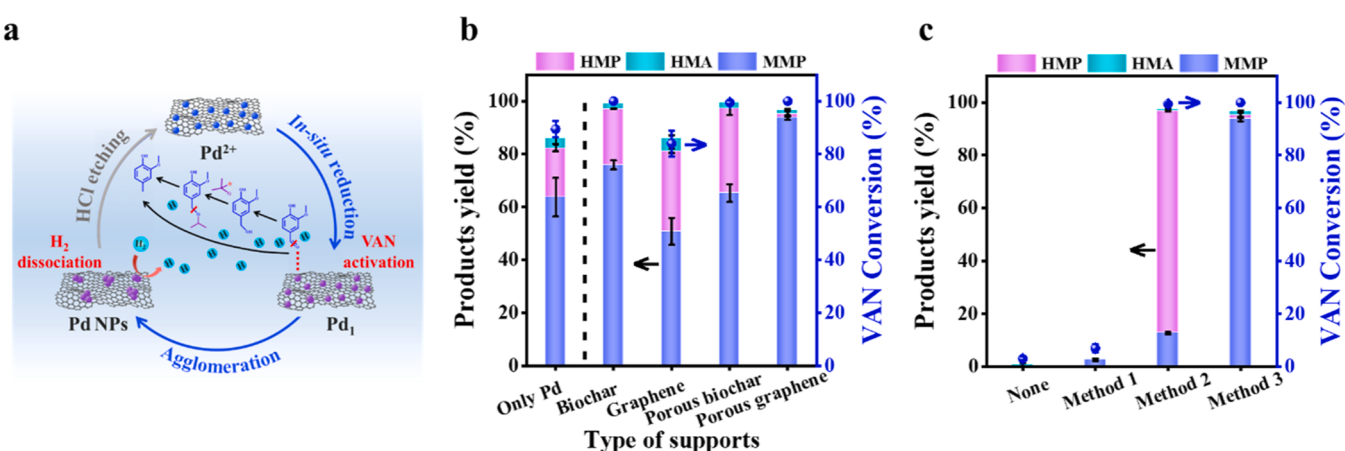


Fig. 1. The proposed working mechanism of the dynamic Pd catalysis and their performance in VAN hydrogenation. (a) Schematic diagram of the dynamic Pd catalysis. (b) Comparison of VAN conversion and MMP yield assisted by biochar, graphene, porous biochar, and porous graphene in the *All-in-one* system. (c) Comparison of hydrogenation efficiency between the dynamic Pd catalysis (method 3) and traditional $NaBH_4$ reduction method (method 1) and H_2 reduction method (method 2). Experimental parameters: 2 mmol VAN, 30 mg 2.5 wt% Pd/Porous graphene, 20 mL IPA, 0.5 MPa H_2 , 30 °C, 30 min.

$$\text{Yield}(\%) = \frac{\text{Wsingle product}}{\text{Wfeedstock}} \times 100\% \quad (2)$$

$$\text{Selectivity}(\%) = \frac{\text{Wsingle product}}{\sum \text{Wsingle product}} \times 100\% \quad (3)$$

The turnover frequency (TOF) and turnover number (TON) were calculated at a near complete VAN conversion (18 min) by following equation:

$$\text{TOF} = \frac{\text{M}_{2-\text{methoxy}-4-\text{methylphenol}}}{(\text{Msurface Pd} \times \text{Time})} \quad (4)$$

$$\text{TON} = \frac{\text{M}_{2-\text{methoxy}-4-\text{methylphenol}}}{\text{Msurface Pd}} \quad (5)$$

2.3. Characterization of Pd loaded porous graphene

Raman spectra was used to analyses the thin sheet structures of support. It was carried out using a XploRA Raman spectrometer with a 532 nm (5 mW) laser source under a 503 objective microscope. And the Raman parameters were fitted with three distinctive Lorentz peaks using Lab-Spec6.4 software, corresponding to G ($\sim 1580 \text{ cm}^{-1}$), D ($\sim 1350 \text{ cm}^{-1}$), and 2D (2700 cm^{-1}) bands, respectively. Valence state changes during the Pd synthesis were recorded using X-ray absorption spectroscopy (XAS) at the Pd K-edge were obtained at the BL14W1 station in Shanghai Synchrotron Radiation Facility, China [34]. The electron storage ring was operated at 3.5 GeV with a maximum current of 250 mA. The acquired extended X-ray absorption fine structure (EXAFS) data were processed according to the standard procedures using the ATHENA module implemented in the IFEFFIT software packages. The quantitative structural information was obtained by least-squares curve fitting using the ARTEMIS module of IFEFFIT software packages. Ultraviolet photoelectron spectroscopy (UPS) was used to determine the ability of the catalyst to gain and lose electrons. It was carried out by an ESCALAB Xi+. The analysis was conducted under a vacuum pressure of $8 \times 10^{-10} \text{ Pa}$ in the analytical chamber. The excitation source used was He I (21.22 eV), and the pass energy for the measurements was set at 50 eV with a step size of 0.05 eV. Charging correction was performed using Au as the energy reference. The spot size of the incident X-ray beam was set to 1 millimeter. DFT calculations were conducted to analyze the effects of Pd₁ and Pd NPs on substrate adsorption and hydrogen dissociation. Briefly, all the computations were implemented with spin-polarized density functional theory (DFT) method, as performed by the Vienna ab initio simulation package (VASP) [35]. The projector augmented wavefunction (PAW) pseudo-potentials are used to describe ionic potentials [35]. The exchange correlation energy is sculptured by Perdew–Burke–Ernzerhof (PBE) functional within the generalized gradient approximation (GGA) [36]. In the course of the geometry relaxation, the energy cut-off was chosen as 500 eV. In structural optimizations, the Brillouin zone are sampled by $3 \times 3 \times 1$ mesh points in k-space based on Monkhorst–Pack scheme both for PdN₄ and Pd NPs, respectively [37]. The force convergence criterion for atomic relaxation is set to be 0.02 eV/Å. The climbing image nudged elastic band (CI–NEB) method is used to search for the transition state for the elementary reaction, and the convergence for the force criterion is set to be 0.03 eV/Å. The vacuum gap is set as 20 Å to preclude interplay between two adjacent surfaces. The adsorption energy (ΔE_{ad}) of VAN, 4-hydroxymethyl–2-methoxyphenol (HMP), 4-hydroxy-3-methoxybenzylalcohol, isopropyl ether (HMA), 2-methoxy-4-methylphenol (MMP) molecules on PdN₄ and Pd NPs were defined as:

$$\Delta E_{ads} = E_{sur+mol} - E_{sur} - E_{mol} \quad (4)$$

Where $E_{sur+mol}$ represents the total energy of the molecule adsorbed structure. E_{sur} represents the total energy of pure PdN₄ or Pd NPs, E_{mol} is the total energy of VAN, HMP, HMA, MMP molecules calculated in a bulk, respectively. Moreover, Transmission electron microscopy (TEM), N₂ adsorption–desorption, elemental analysis, inductively coupled plasma optical emission spectroscopy (ICP–OES), and hydrogen temperature-programmed reduction (H₂-TPR) were also determined to

characterize the catalyst. Detailed information can be found in Supporting Information (Section 1.5).

3. Results and discussion

3.1. Porous graphene confined Pd size in the All-in-one system for hydrogenation

Porous graphene was used to confine Pd for hydrogenation and synthesized via emerging flash Joule heating reaction of porous carbon (Fig. S1). The millisecond ultra-high temperature (up to 3000 °C) in flash Joule heating reaction induced the graphitization of carbon skeletton, and simultaneous electrical exfoliation function promoted the formation of porous graphene (Fig. S2, S4) [38,39]. It should be noted that the porosity of porous graphene was due to the retention of its precursor. Obviously, as-prepared porous graphene has both distinct 2D peaks and high surface area characteristics ($2118.0 \text{ m}^2/\text{g}$). Accordingly, the high surface area also resulted in the low N density (0.001 N/m^2), which is promising for Pd anchoring (Fig. S5–S6). VAN, a model lignin aldehyde compound, was used as the substrate to evaluate the hydrogenation efficiency of Pd. A dynamic All-in-one system, distinct from traditional static catalysis, is characterized by the integration of Pd anchoring and *in-situ* reduction, as well as substrate conversion. As shown in Figs. 1b–1c, complete conversion of VAN to the desired product MMP was achieved with a yield of $> 95.0\%$ with porous graphene as the carbon support in the All-in-one system. Furthermore, the TOF and TON of 488.6 min^{-1} and 8793.9 were achieved. Notably, both carbon support and reaction system significantly influenced hydrogenation efficiency. Specifically, porous graphene was found to enhance MMP yield, which may be due to the favorable confinement of Pd caused by its low N density (0.001 N/m^2). Besides, it is speculated that the dynamic integration of Pd reduction and substrate conversion process in the All-in-one system may also enhance the hydrogenation efficiency. In addition, the potential catalytic effects of Pd²⁺, Cl[−], and the acidity were ruled out by appropriate experiments (Table S1–S2, entries 1–3). Furthermore, elevated reaction temperature and time, increased Pd loading, and the participation of excess hydrogen, along with the isopropanol as a solvent greatly enhance VAN conversion and MMP yield (Fig. S7–S11).

As shown in Fig. 1b, porous graphene is highly desirable for use as a support to anchor Pd as its low-density N concentration (0.001 N/m^2) resulting from large specific areas ($2118.0 \text{ m}^2/\text{g}$) and thin sheets (Table S3). To substantiate Pd anchoring and reduction, the rapid stabilization of Pd²⁺ ions on porous graphene is first demonstrated. Almost complete Pd²⁺ ions ($\sim 99.3\%$) can be immobilized on porous graphene in the All-in-one system before reaction (Fig. S12). The All-in-one system facilitates the expeditious reduction of Pd²⁺ ions to Pd⁰ (Fig. S13). In order to further explore Pd reduction in the All-in-one system, the post-reaction catalyst was characterized. Catalysts using porous biochar and porous graphene displayed type-IV isotherms, indicating the presence of both microporous and mesoporous structures (Fig. 2a) [40]. Remarkably, the catalyst obtained by employing porous graphene had large specific surface areas ($1992.7 \text{ m}^2/\text{g}$) and pore volume ($1.12 \text{ cm}^3/\text{g}$), as well as distinct 2D peak (Figs. 2a–2b, Fig. S14). Therefore, the highly dispersed Pd NPs with an average particle size of 2.1 nm on porous graphene in the All-in-one system was observed in Figs. 2c–2e and Table S4–S5. This can be attributed to the enough N sites offered by porous graphene with N-doping for Pd anchoring ($n_N:n_{pd} = 6:1$), consequently restricting the further aggregation of Pd species (Figs. 2d–2e). Moreover, the peaks centered at 62 °C and 65 °C in the H₂-TPR profiles of porous biochar and porous graphene were assigned to the reduction of Pd²⁺ ions, indicating the strong interaction between Pd and N-doping materials (Fig. 2f) [41,42]. It can be inferred that the interaction between Pd and four supports in the All-in-one system followed the same principle. This finding was consistent with the smaller particle size of the post-reaction Pd NPs on porous carbon supports, as

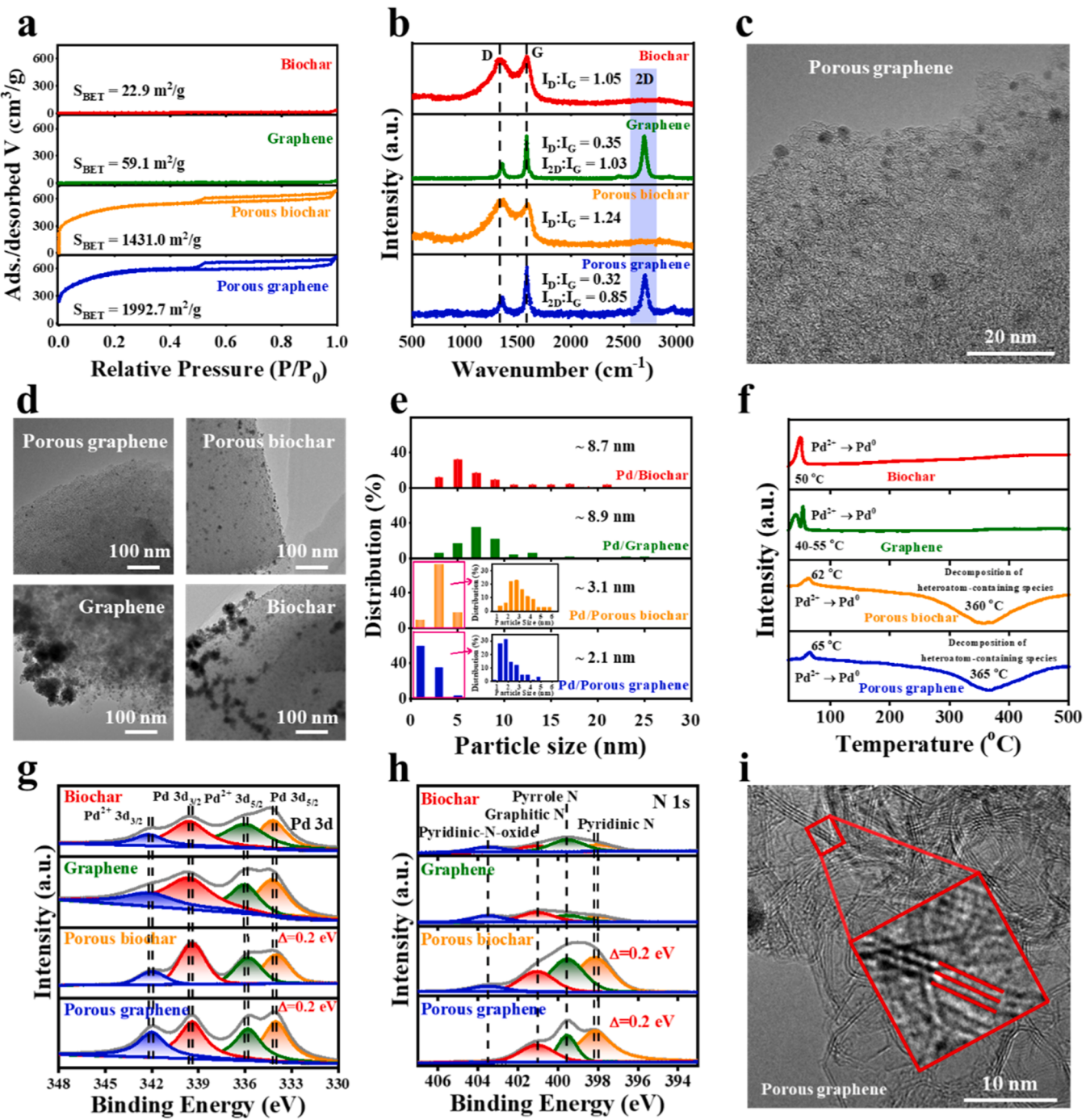


Fig. 2. Morphology and surface chemical property analysis. (a) Nitrogen adsorption–desorption isotherm of Pd/Biochar, Pd/Graphene, Pd/Porous biochar, and Pd/Porous graphene. (b) Raman spectrum of Pd/Biochar, Pd/Graphene, Pd/Porous biochar, and Pd/Porous graphene. (c and d) Transmission electron microscopy (TEM) images of Pd/Porous graphene. (e) Size distributions of Pd NPs. (f) H₂-Temperature Programmed Reduction (H₂-TPR) profiles of Pd/Biochar, Pd/Graphene, Pd/Porous biochar, and Pd/Porous graphene. (g and h) X-ray photoelectron spectroscopy (XPS) N 1s and Pd 3d spectrum of Pd/Biochar, Pd/Graphene, Pd/Porous biochar, and Pd/Porous graphene. (i) HR-TEM images of thin sheet structures in Pd/Porous graphene.

illustrated in the Pd size distributions (Fig. 2e). However, due to the lack of uniformly N-doping caused by large specific surface areas in biochar and graphene, larger Pd NPs exceeding 8.7 nm in size and their severe agglomeration are discernible (Fig. 2a, Figs. 2d–2e, Fig. S15–S17, Table S5). Besides, the higher density of N (0.005% N/m²) and lack of thin sheets structure in porous biochar caused slightly Pd agglomeration (3.1 nm) (Fig. 2b, Figs. 2d–2e, Fig. S18, Table S5).

In addition, N-doping in porous graphene also modulates the charge distribution on the Pd surface, thereby enhancing its anchoring. Briefly,

Pd has lower binding energy (BE), while pyridinic-N showed the higher BE onto N-doping supports ($\Delta=0.2 \text{ eV}$), indicating electron transfer from pyridinic-N to Pd (Figs. 2g–2h, Table S6–S7) [43,44]. Moreover, this modulation also could promote the adsorption of substrates on Pd sites. This is because the electron-deficient carbocation intermediates in aromatic carbonyl groups are stabilized by the electron-donating pyridinic-N [28,41,45]. HR-TEM images reveal distinct sheets structures in porous graphene (Fig. 2i), which could also promote the activation of α -carbon in VAN molecules through π - π interactions, thus

endowing the excellent activity for VAN conversion [27,46,47]. It has been extensively documented that small-sized Pd NPs possess the capability to enhance hydrogenation reactions [26,41,42,48]. Therefore, as shown in Fig. 1b, the small-sized Pd NPs (2.1 nm) on porous graphene promoted 100% conversion of VAN to >95% yield of MMP in the *All-in-one* system. In comparison, Pd NPs on porous biochar exhibited a slightly larger size (3.1 nm), contributing to a yield of 65.30% for MMP. Nevertheless, the activity of Pd in the liquid phase without carbon support was relatively high, resulting in an MMP yield of 63.74%. Thus, despite the large Pd particle size of 8.7 nm, the MMP yield on biochar reached 75.94% due to its low Pd loading (only 1.08 wt%, Table S5). In contrast, the agglomeration of Pd on graphene was severe (with a Pd particle size of 8.9 nm), and the Pd loading was high (1.68 wt%, Table S5). Consequently, there were fewer active sites both on the support and in the solution, resulting in its lowest MMP yield (only 50.83%). Overall, considering the advantages of porous graphene in Pd confinement and recovery, porous graphene-assisted *All-in-one* system was believed to be superior for hydrogenation.

3.2. Dynamic Pd size assisted by porous graphene for high hydrogenation activity

It should be noticed that the Pd catalyst synthesized by H₂ reduction exhibited the smallest Pd particle size of 1.1 nm, the largest specific surface area of 2024.2 m²/g and the same N density of 0.001% N/m² (Fig. S19–S23). Besides, the distinct diffraction peaks of Pd in the XRD pattern and the observed peak of Pd⁰ in the XPS spectrum both prove that H₂ reduction can successfully realize the loading and reduction of Pd on porous graphene (Fig. S24–S25). However, the MMP yield by using this catalyst was only 12.6%. Therefore, it can be speculated that traditional statically immobilized Pd NPs has poor catalytic hydrogenation activity. In contrast, the enhanced efficiency in the *All-in-one* system may originate from the distinctive catalytic effect generated by the dynamic integration of Pd reduction and substrate conversion processes. To further confirm Pd⁰ growth on porous carbon in the *All-in-one* system, time-series analyses of Pd valence states and its coordination environment were conducted (Figs. 3a–3b, Table S8). Because the effective reduction of Pd²⁺ ions in the *All-in-one* system has been confirmed above, 1 min was selected as a representative sample to

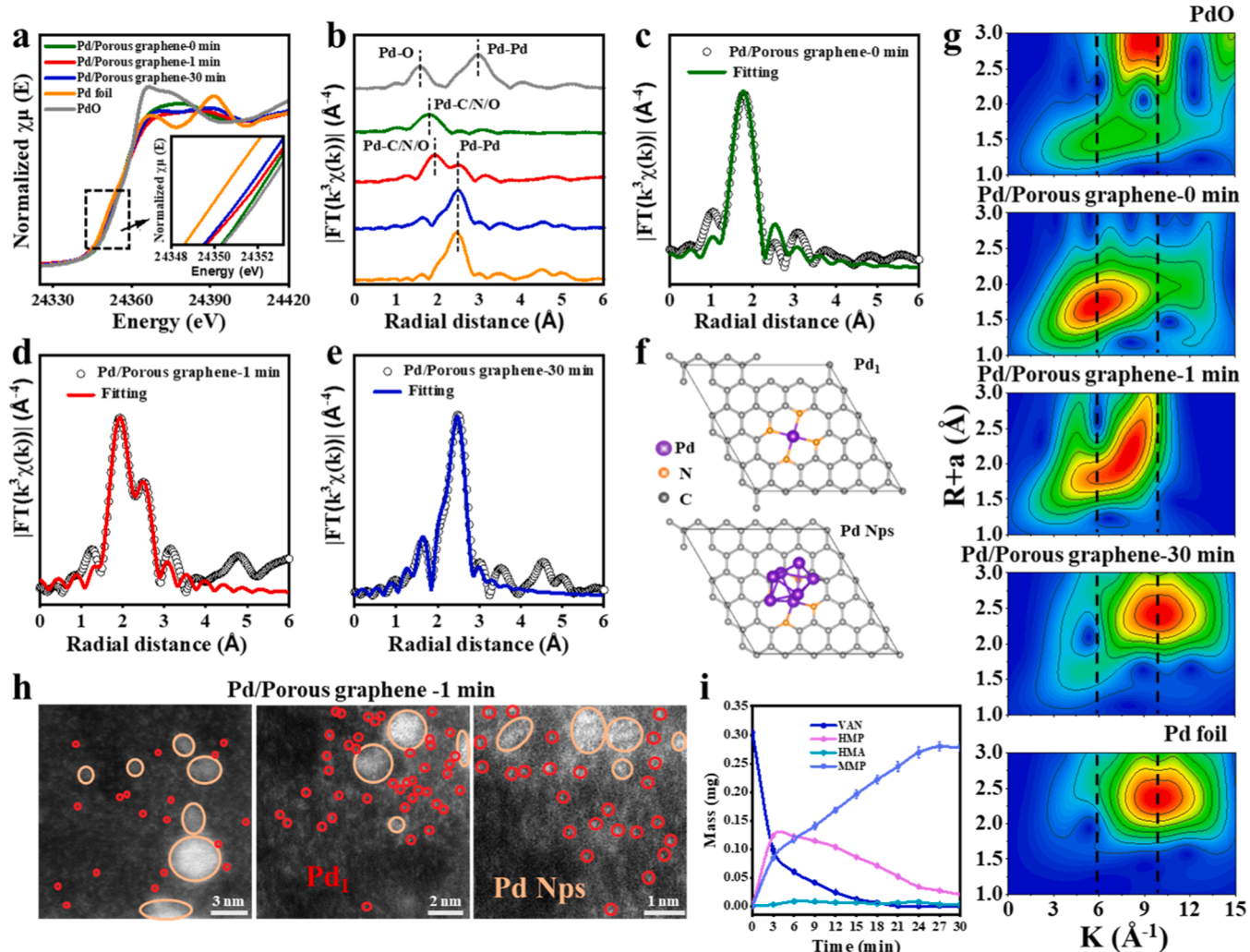


Fig. 3. Pd valence state and coordination environment in dynamic Pd reduction process. (a) Pd K-edge X-ray absorption near-edge structure (XANES) spectra of Pd foil, PdO, and Pd/Porous graphene at 0, 1 and 30 min of reduction. (b) FT k³-weighted Pd K-edge extended X-ray absorption fine structure (EXAFS) spectra of Pd foil, PdO, and Pd/Porous graphene at 0, 1 and 30 min of reduction. (c-e) EXAFS fitting curve of Pd/Porous graphene at 0, 1 and 30 min of reduction. (f) Pd₁ and Pd NPs models of the corresponding calculated spectra (The purple, orange, and gray spheres represent Pd, N, and C atoms, respectively). (g) Pd K-edge wavelet transform (WT)-EXAFS for Pd foil, PdO, and Pd/Porous graphene at 0, 1 and 30 min of reduction. (h) High-angle annular dark-field (HAADF) images of Pd/Porous graphene at 1 min of reduction with red circle highlighted Pd₁ and orange circle highlighted Pd NPs. (i) High pressure in-situ quantitative analysis of VAN and its products. Experimental parameters: 2 mmol VAN, 30 mg 2.5 wt% Pd/Porous graphene, 20 mL IPA, 0.5 MPa H₂, 30 °C.

compare the intermediate states of Pd with Pd before reduction (0 min) and after reduction (30 min). As expected, the X-ray absorption near-edge structure (XANES) spectra indicate a rapid reduction of Pd^{2+} from Pd_1 to Pd NPs (Fig. 3a, Fig. S26–S27). Furthermore, a slightly higher oxidation state was assigned to Pd^{2+} before reduction, indicating the robust interaction between Pd and N in the porous graphene, which

aligns with the conclusions in the preceding section. The R spaces from extended X-ray absorption fine structure (EXAFS) curves exhibited a peak only around 2.2 Å, confirming the uniqueness of the PdN_4 coordination (Figs. 3b, 3c and 3f) [49]. This further confirmed the above conclusion that Pd coordinates well with N in porous graphene. Correspondingly, two main peaks at 2.2 and 2.7 Å that can be assigned to

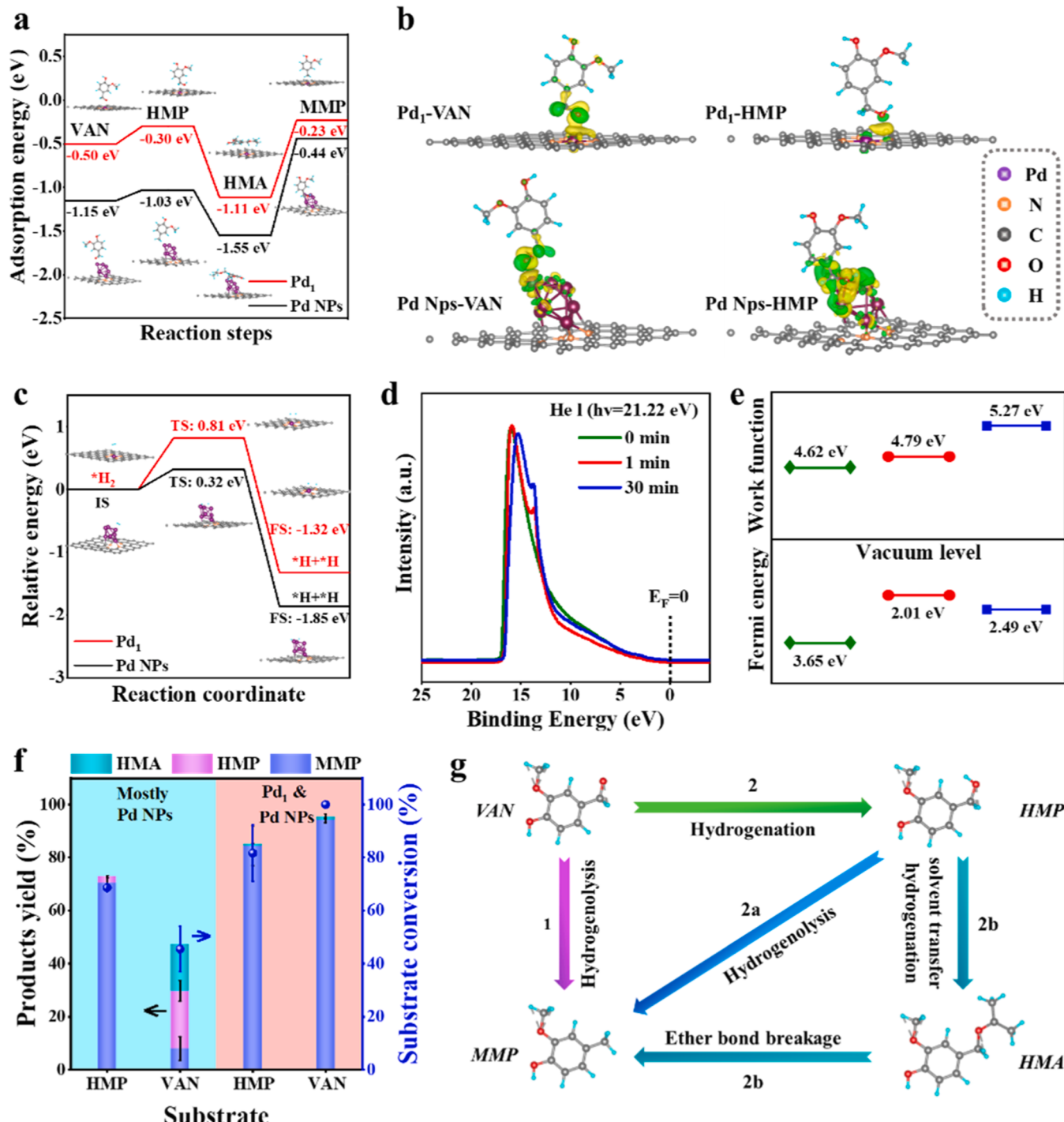


Fig. 4. Reaction mechanism of the dynamic Pd catalysis for hydrogenation. (a) Density functional theory (DFT) calculation of VAN, HMP, HMA and MMP coordinated with Pd_1 (red line) and Pd NPs (black line). (b) DFT calculation of charge–density difference in VAN and HMP adsorbed on Pd_1 and Pd NPs. The green and yellow isosurfaces represent the charge accumulation and depletion region, respectively. (c) DFT calculation of H_2 dissociation on Pd_1 and Pd NPs. (d) UPS spectrum of Pd/Porous graphene at 0, 1 and 30 min of reduction. (e) The Work function and Fermi levels of Pd/Porous graphene at 0, 1 and 30 min of reduction. (f) The VAN and HMP as substrate in *All-in-one* system (intergraded Pd reduction and substrate conversion) and the separated system (NPs were synthesized first and then the substrate were added). Experimental parameters: 2 mmol VAN or HMP, 30 mg 2.5 wt% Pd/Porous graphene, 20 mL IPA, 0.5 MPa H_2 , 30 °C, 30 min. (g) Possible reaction pathways for VAN hydrogenation.

Pd–N and Pd–Pd bonds, respectively (Figs. 3b and 3d), conforming the co-existence of Pd₁ and Pd NPs after 1 min of H₂ reduction. Plenty of Pd₁ and Pd NPs in high-angle annular dark-field (HAADF) images also coincided with the above results (Fig. 3h). Moreover, Pd NPs was indicated by the obvious peak at 2.7 Å after 30 min of reduction, which reflecting Pd₇ nanoparticles were generated by aggregation of Pd₁ (Figs. 3b, 3e and 3f) [50]. In addition, the Pd–Pd coordination number increased from 0 prior to the reduction to 1.3 at 1 min and eventually reaching 4.8 at 30 min. This further indicates the growth of Pd₁ to Pd NPs over time (Table S8). Consequently, it can be concluded that Pd grow gradually from atomically distributed Pd₁ to the co-existence of Pd₁ and Pd NPs, and finally grow into predominantly Pd NPs (Fig. S28). Additionally, the maximum intensity of Pd in wavelet transform EXAFS analysis increased from 5.9 Å⁻¹ (attributed to Pd–N) to 9.8 Å⁻¹ (attributed to Pd–Pd), further demonstrating the evolution of Pd species from Pd²⁺ to Pd⁰ (Fig. 3g). The mass of HMP increased firstly and then decreased, indicating that it was an intermediate product in VAN hydrogenation (Fig. 3i). The dramatic mass changes of VAN and the inflection point of its intermediate product (HMP) during the initial stage of the reaction correspond to the co-existence of Pd₁ and Pd NPs, which further confirmed their synergistic effects on VAN hydrogenation (Fig. 3i). It was proposed that Pd₁ and Pd NPs might exhibit distinct catalytic roles in the activation and hydrogenation of VAN. In contrast, more Pd NPs and fewer Pd₁ were observed by employing graphene as a support in HAADF images proved that Pd₁ cannot be well confined due to the lack of N in graphene (Fig. S29). The lower coordination number of Pd–N (1.8) and the higher coordination number of Pd–Pd (11.3) also reflected the more big-sized Pd NPs dispersed on graphene, thereby impedes the hydrogenation of VAN to MMP (Table S8, Fig. S30).

To summarize, Pd²⁺ almost completely distributed onto porous graphene atomically and reduced to Pd₁ in the beginning, and progressively agglomerated to Pd NPs. During this process, VAN was converted simultaneously and ultimately yield MMP through the synergistic activity of Pd₁ and Pd NPs.

3.3. Mechanism study of the dynamic Pd catalysis for vanillin hydrogenation

To theoretically unravel the role of Pd₁ and Pd NPs, substrate adsorption and H₂ dissociation were studied using density functional theory (DFT) calculation based on the two models shown in Fig. 3f. The much higher adsorption energy of the substrates on Pd NPs than on Pd₁ indicated the induced enhancement for substrates adsorption on Pd NPs (Fig. 4a), which is consistent with the deformation charge density in Fig. 4b. Nonetheless, their activity may be impeded by either inadequate or excessive substrate binding to the surface, which impedes their capture or detachment, respectively [51]. Hence, equilibrium between the adsorption and desorption of the substrate was more easily reached on Pd₁, which is consistent with the conclusion of Li et al. [49]. Usually, homolytic cleavage of H₂ requires a lower activation energy and is more likely to occur on metal [16]. In order to further investigate the H₂ dissociation energy on Pd₁ and Pd NPs, the essential steps were conducted, as shown in Fig. 4c. The higher barrier on Pd₁ (0.8 eV) compared to Pd NPs (0.3 eV) suggested that Pd NPs contributes more on H₂ dissociation than Pd₁. Overall, it can be concluded that Pd₁ activates VAN, whereas Pd NPs contributes more on the generation of H[•], which attack VAN to produce MMP.

To verify the above conclusion, ultraviolet photoelectron spectrometry (UPS) was performed to analyze the electron gain/loss ability and reactivity of catalyst in dynamic Pd catalysis (Fig. 4d). The work function of Pd reduced in the *All-in-one* system assisted by porous graphene gradually increased from 4.6 eV to 5.3 eV as the reduction time increased, indicating the electrons acquisition process of Pd²⁺ ions reduction (Fig. 4e). Furthermore, the lowest Fermi energy reflects the highest active catalyst at 1 min of reduction (2.0 eV, Fig. 4e). This further verifies that the coexistence of Pd₁ and Pd NPs has the highest

catalytic activity, that is, Pd₁ and Pd NPs have the synergistic effects.

Based on the previous reports on the conversion of VAN to MMP, direct hydrogenation (path 1) and indirect hydrogenation (path 2-2a and path 2-2b) of VAN are proposed in Fig. 4g [52,53]. To determine the contributions of Pd₁ and Pd NPs to each step of VAN conversion, VAN and its intermediate product (HMP) were used as substrates for different stages of dynamic Pd catalysis. Specifically, Pd NPs played a prominent role during the separated Pd reduction and reactant hydrogenation process. In contrast, Pd₁ and Pd NPs have the synergistic effects in the integrated *All-in-one* system. HMA was inferred to be the product of solvent transfer hydrogenation between HMP and isopropanol based on its molecular structure. The occurrence of the transfer hydrogenation reaction was also confirmed by Paul, et al. [54]. However, the HMA yield in Fig. 1b–c was lower than 4.93%, and the mass of HMA was ranged from 0.002 to 0.008 g as depicted in Fig. 3i, indicating that path 2-2b was not the primary pathway. A significant MMP yield of 70.3% was achieved during the separated Pd reduction and HMP hydrogenation process, which strongly suggested the predominant effects of Pd NPs in path 2a. In contrast, only 8.1% of MMP yield was obtained using VAN as the substrate. It can be inferred that Pd NPs cannot promote path 2 and path 1. In addition, the activation of VAN was limited due to the lack of Pd₁, resulting in difficulty in VAN conversion. Consequently, H[•] generated by Pd NPs promoted the VAN conversion of only 45.55%. The excessive consumption of H[•] presented a challenge for the further hydrogenation of HMP, leading to its accumulation (the HMP yield was 21.75%). However, HMP could converted into HMA through solvent transfer hydrogenation, with isopropanol serving as the hydrogen donor [54]. Consequently, a yield of 17.54% HMA was achieved in this reaction. On the other hand, MMP yield was 84.4% in the *All-in-one* system, while Pd NPs-catalyzed hydrogenation produced 70.3% yield of MMP with HMP as substrate, indicating the less contribution of Pd₁ in path 2a. For path 2 and path 1, it can be inferred that Pd₁ and Pd NPs jointly promote both or only one of them. Therefore, it can be concluded that Pd₁ contributed to path 2 and/or path 1, while Pd NPs played major catalytic roles in path 2a (Figs. 4f–4g). The above conclusion also confirmed the synergistic effects of Pd₁ and Pd NPs. Accordingly, as depicted in Fig. 3i for the *in-situ* monitoring of reactants changes, the initial stage of the reaction corresponded to the co-existence of Pd₁ and Pd NPs, which had synergistic effects on VAN hydrogenation. Pd₁ promoted path 2 and/or path 1, resulting in the conversion of most VAN to HMP and MMP. As the reaction time prolongs, Pd₁ gradually aggregated into Pd NPs, dissociating H₂ to generate H[•]. H[•] promoted further hydrogenation of HMP to generate MMP. Furthermore, the stability of the *All-in-one* system was poor due to the lack of Pd₁ in the recyclability test (Fig. S31). Considering the strong anchoring effect of Pd on porous graphene, most Pd can be recovered after the initial reaction (Fig. S12). The recovered Pd NPs can be converted into Pd²⁺ through the industrial production (HCl etching) for the next catalytic reaction.

3.4. Flexibility of the dynamic Pd catalysis for bio-oil and unsaturated substrates

To investigate the broad-spectrum value of dynamic Pd catalysis, its activity on lignin-derived bio-oil was studied. As shown in Fig. 5a, the increased yield of hydrogenated products reflected that hydrogenation reactions occurred in aromatic compounds containing C=C and C=O in their side chains, including VAN, coniferyl alcohol, and methyl 3-(4-hydroxy-3-methoxyphenyl) propionate. In addition, it also shows high hydrogenation efficiency for 2-phenoxy-1-phenylethanol with a β-O-4 bond. Furthermore, the total monomer yield increased as the temperature increased, indicating depolymerization of the complex multimers. Moreover, a Van Krevelen plot demonstrated the hydrogenation occurred during Pd catalysis of lignin bio-oil, mainly including a decarbonylation reaction (Fig. 5b). Additionally, the color of the hydrogenation products lightened, suggesting the elimination of chromophoric functional groups, including hydroxyl and carbonyl groups

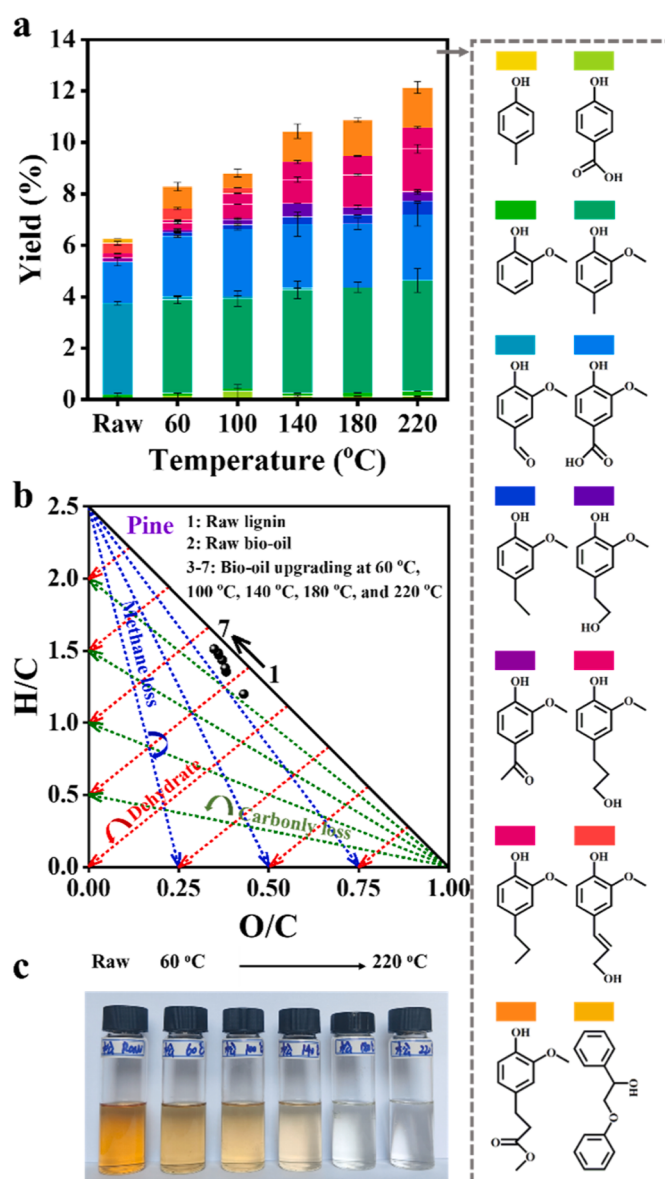


Fig. 5. Flexibility of the dynamic Pd catalysis. (a) The yield of aromatic monomers in the dynamic Pd catalysis from pine bio-oil obtained by microwave-assisted hydrothermal liquefaction (M-HTL). Microwave pyrolysis parameters: 0.2 g lignin, 0.1 mL 30 wt% H_2O_2 , 10 mL 1 M KOH solution, 180 °C, 30 min. The dynamic Pd hydrogenation parameters: 0.03 g 2.5 wt% Pd/Porous graphene, 20 mL isopropanol, 30 min, 0.5 MPa H_2 . (b) Van Krevelen plot of pine bio-oil upgrading in the dynamic Pd hydrogenation. (c) The picture of aromatic monomers from pine bio-oil. (d) The dynamic Pd catalysis for various unsaturated chemicals hydrogenation. ^a: 2 mmol substrate. ^b: 0.5 mmol substrate.

(Fig. 5c). Overall, it can be concluded that the dynamic Pd catalysis exhibits remarkable activity, even in such real complex reaction.

To further investigate the flexibility of the dynamic Pd catalysis, a barrage of unsaturated compounds containing functional groups with C=C, C=O, and -NO₂ were proven to be applicable (Fig. 5d). (1) C=C in the side chain of aromatic compounds were easily hydrogenated in high yields at close to room temperature (Entries 1–3). (2) the hydrogenation of aldehydes, including benzyl and aliphatic aldehydes, are more challenging (Entries 4–9). In terms of benzyl aldehydes, they were successfully converted into the desired deoxygenated products, such as benzaldehyde, p-hydroxybenzaldehyde, VAN, and acetovanillone, at temperatures lower than 80 °C (Entries 4–7). In contrast, aliphatic aldehydes were mostly converted into their corresponding alcohols owing to the unique stabilizing effect of the electron-donating phenyl groups on the involved carbo-cation intermediates (Entries 8–9) [6]. (3) Due to the steric effect of -CH₃ and electron-absorbing effect of the double -OCH₃, hydrogenation of the keto group in the side chain required more

harsh conditions such as higher catalyst dosage and/or temperatures (Entries 10–15). (4) The dynamic Pd catalysis also exhibited superior catalytic performance for nitrobenzene conversion, achieving nearly complete conversion with a remarkable 99.9% yield of valuable aniline (Entries 16). These hydrogenation products are important reagents for the preparation of pharmaceuticals, flavors, and cosmetics in the fine chemical industry [55,56]. Therefore, the successful hydrogenation of lignin bio-oil and C=C, C=O, and -NO₂ demonstrates broader application value for the dynamic Pd catalysis in more challenging hydrogenation reactions in the petrochemical industry (Fig. S32).

Overall, compared with the traditional H_2 and NaBH₄ reduction method, the *All-in-one* system could take advantage of the dynamic Pd size for hydrogenation. Thus, its atom efficiency was high. Moreover, the *All-in-one* system was a very simple and rapid method because it allowed for rapid and extensive screening and optimization of Pd catalysts with freely tunable Pd contents to improve the catalytic activity for hydrogenation.

4. Conclusion

This work presents a novel dynamic Pd catalysis assisted by porous graphene in an *All-in-one* system for hydrogenation. Porous graphene with N-doping was employed as the carbon support to confine Pd and active substrate due to its thin sheets and uniform N-doping caused by its large specific surface areas. The *All-in-one* system exhibited excellent activity owing to the synergistic effects of Pd₁ and Pd NPs. Specifically, the initially formed Pd₁ first activated the substrate, and then aggregated into Pd NPs to promote H₂ dissociation. The generated active hydrogen promoted the conversion of the substrate into its hydrogenated products. The flexibility of *All-in-one* system for complex lignin bio-oils and broad-spectrum unsaturated substrates under mild conditions was also confirmed. Overall, this study not only presents a prospective approach for unsaturated substrate hydrogenation, but also advances the comprehension of the mechanism underlying the dynamic Pd catalysis.

CRediT authorship contribution statement

Lina Li: Writing – review & editing. **Chao Jia:** Writing – original draft. **Yong Wang:** Conceptualization, Writing – review & editing. **Fengbo Yu:** Resources, Investigation, Formal analysis. **Xiangdong Zhu:** Conceptualization, Resources, Supervision, Writing – review & editing. **Yang Cao:** Resources, Investigation, Formal analysis. **Shicheng Zhang:** Funding acquisition, Methodology, Resources, Supervision, Writing – review & editing. **Linyu Zhu:** Visualization, Software, Data curation. **Aodi Li:** Visualization, Software. **Liming Sun:** Resources, Investigation, Formal analysis. **Litao Lin:** Visualization. **Xuan Wu:** Resources, Investigation. **Zhelin He:** Data curation, Resources. **Zhongyue Zhou:** Writing – review & editing. **James H. Clark:** Writing – review & editing. **Jie Gao:** Writing – original draft, Visualization, Methodology, Investigation, Formal analysis, Data curation, Conceptualization.

Declaration of Competing Interest

The authors declare that they have no known competing financial interests or personal relationships that could have appeared to influence the work reported in this paper.

Data availability

No data was used for the research described in the article.

Acknowledgements

The authors acknowledge the financial support from the National Natural Science Foundation of China (No. 22278085). The authors thank beamline BL14W1 (Shanghai Synchrotron Radiation Facility) for providing the beam time. The authors thank the DFT calculations assisted by Shenzhen HUASUAN Technology Co., Ltd. The authors thank Chunfang Zheng (Shiyanjia Lab, www.shiyanjia.com) for the support of the XRD and XPS test.

Appendix A. Supporting information

Supplementary data associated with this article can be found in the online version at [doi:10.1016/j.apcatb.2024.124026](https://doi.org/10.1016/j.apcatb.2024.124026).

References

- [1] A.J. Ragauskas, G.T. Beckham, M.J. Biddy, R. Chandra, F. Chen, M.F. Davis, B. H. Davison, R. ADixon, P. Gilna, M. Keller, Lignin valorization: improving lignin processing in the biorefinery, *Science* 344 (2014) 1246843, <https://doi.org/10.1126/science.1246843>.
- [2] H.H. Ning, Y.Z. Chen, Z.Z. Wang, S.J. Mao, Z.R. Chen, Y.T. Gong, Y. Wang, Selective upgrading of biomass-derived benzylidic ketones by (formic acid)-Pd/HPC-NH₂ system with high efficiency under ambient conditions, *Chem* 7 (2021) 1–16, <https://doi.org/10.1016/j.chempr.2021.07.002>.
- [3] X.J. Guo, Z.C. Jiang, Y. Ma, J.J. Fan, J.H. Clark, W.H. Zhang, B. Shi, Co-self-assembly of lignin and tannin: a novel catalyst support for hydrogenation of lignin-derived aldehydes, *Appl. Catal. B-Environ.* 339 (2023) 123175, <https://doi.org/10.1016/j.apcatb.2023.123175>.
- [4] H. Xu, H. Li, Regulating the crystal phase of Pd/Nb₂O₅ for vanillin selective HDO at room temperature, *J. Catal.* 423 (2023) 105–117, <https://doi.org/10.1016/j.jcat.2023.04.010>.
- [5] A.E. King, T.J. Brooks, Y.-H. Tian, E.R. Batista, A.D. Sutton, Understanding ketone hydrodeoxygenation for the production of fuels and feedstocks from biomass, *ACS Catal.* 5 (2015) 1223–1226, <https://doi.org/10.1021/cs501965w>.
- [6] B. Demira, T. Kropka, K.R. Rivera-Donesa, E.B. Gilchera, G.W. Hubera, M. Mavrikakisa, J.A. Dumesic, A self-adjusting platinum surface for acetone hydrogenation, *Proc. Natl. Acad. Sci. U. S. A.* 117 (2020) 3446–3450, <https://doi.org/10.1073/pnas.1917110117>.
- [7] C.Z. Chen, X.L. Ji, Y.Z. Xiong, J.C. Jiang, Ni/Ce co-doping metal-organic framework catalysts with oxygen vacancy for catalytic transfer hydrodeoxygenation of lignin derivatives vanillin, *Chem. Eng. J.* 481 (2024) 148555, <https://doi.org/10.1016/j.cej.2024.148555>.
- [8] J.J. Luo, M.S. Sun, B.Y. Tang, Y. Zhou, W.T. Chen, W.Q. Gong, S. Han, F.F. Mao, Z. M. Li, D.J. Tao, Solvent-controlled product distribution in vanillin hydrogenation over a N-doped carbon-supported nickel catalyst, *Ind. Eng. Chem. Res.* 62 (2023) 9134–9143, <https://doi.org/10.1021/acs.iecr.3c00510>.
- [9] L. Kuai, Z. Chen, S.J. Liu, E. Kan, N. Yu, Y.M. Ren, C.H. Fang, X.Y. Li, Y.D. Li, B. Y. Geng, Titania supported synergistic palladium single atoms and nanoparticles for room temperature ketone and aldehydes hydrogenation, *Nat. Commun.* 11 (2020) 48, <https://doi.org/10.1038/s41467-019-13941-5>.
- [10] F.R. Lucci, M.T. Darby, M.F.G. Mattera, C. Ivimey, A.J. Therrien, A. Michaelides, M. Stamatakis, E.C.H. Sykes, Controlling hydrogen activation, spillover, and desorption with Pd-Au single-atom alloys, *J. Phys. Chem. Lett.* 7 (2016) 480–485, <https://doi.org/10.1021/acs.jpclett.5b02400>.
- [11] C.P. Wang, S.J. Mao, Z. Wang, Y.Z. Chen, W.T. Yuan, Y. Ou, H. Zhang, Y.T. Gong, Y. Wang, Insight into single-atom-induced unconventional size dependence over CeO₂-supported Pt catalysts, *Chem* 6 (2020) 752–765, <https://doi.org/10.1016/j.chempr.2019.12.029>.
- [12] Q.K. Shen, H.Q. Jin, P.P. Li, X.H. Yu, L.R. Zheng, W.G. Song, C.Y. Cao, Breaking the activity limitation of iridium single-atom catalyst in hydrogenation of quinoline with synergistic nanoparticles catalysis, *Nano Res* 15 (2022) 5024–5031, <https://doi.org/10.1007/s12274-022-4235-4>.
- [13] P.X. Liu, Y. Zhao, R.X. Qin, S.G. Mo, G.X. Chen, L. Gu, D.M. Chevrier, P. Zhang, Q. Guo, D.O. Zang, Photochemical route for synthesizing atomically dispersed palladium catalysts, *Science* 352 (2016) 797–800, <https://doi.org/10.1126/science.aaf5251>.
- [14] J.Y. Liu, Catalysis by supported single metal atoms, *ACS Catal.* 7 (2016) 34–59, <https://doi.org/10.1021/acscatal.6b01534>.
- [15] L. Kuai, L. Liu, Q.M. Tao, N. Yu, E.J. Kan, N. Sun, S.J. Liu, B.Y. Geng, High-areal density single-atoms/metal oxide nanosheets: a micro-gas blasting synthesis and superior catalytic properties, *Angew. Chem. -Int. Ed.* 134 (61) (2022) e2022, <https://doi.org/10.1002/ange.20221238>.
- [16] X.L. Jiang, F.-T. Sheng, Y. Zhang, G. Deng, S.L. Zhu, Ligand relay catalysis enables asymmetric migratory reductive acylation of olefins or alkyl halides, *J. Am. Chem. Soc.* 144 (2022) 21448–21456, <https://doi.org/10.1021/jacs.2c10785>.
- [17] D.L. Golden, C.F. Zhang, S.-J. Chen, A. Vasilopoulos, I.A. Guzei, S.S. Stahl, Benzylidic C-H esterification with limiting C-H substrate enabled by photochemical redox buffering of the Cu catalyst, *J. Am. Chem. Soc.* 145 (2023) 9434–9440, <https://doi.org/10.1021/jacs.3c01662>.
- [18] X. Chang, X. Cheng, X.-T. Liu, C. Fu, W.-Y. Wang, C.-J. Wang, Stereodivergent construction of 1,4-nonadjacent stereocenters via hydroalkylation of racemic allylic alcohols enabled by copper/ruthenium relay catalysis, *Angew. Chem. -Int. Ed.* 61 (2022) e202206517, <https://doi.org/10.1002/anie.202206517>.
- [19] T. Wang, X.Q. Tao, X., L. Li, K. Zhang, S.J. Liu, B.X. Li, Synergistic Pd single atoms, clusters, and oxygen vacancies on TiO₂ for photocatalytic hydrogen evolution coupled with selective organic oxidation, *Small* 17 (2021) e2006255, <https://doi.org/10.1002/smll.202006255>.
- [20] H.J. Jeong, O. Kwon, B.-S. Kim, J.M. Bae, S.Y. Shin, H.-E. Kim, J.H. Kim, H. Lee, Highly durable metal ensemble catalysts with full dispersion for automotive applications beyond single-atom catalysts, *Nat. Catal.* 3 (2020) 368–375, <https://doi.org/10.1038/s41929-020-0427-z>.
- [21] X.B. Fan, G.L. Zhang, F.B. Zhang, Multiple roles of graphene in heterogeneous catalysis, *Chem. Soc. Rev.* 44 (2015) 3023–3035, <https://doi.org/10.1039/c5cs00094g>.
- [22] S.J. Wan, J.S. Xu, S.W. Cao, J.G. Yu, Promoting intramolecular charge transfer of graphitic carbon nitride by donor-acceptor modulation for visible-light photocatalytic H₂ evolution, *Interdiscip. Mater.* 1 (2022) 294–308, <https://doi.org/10.1002/itm2.12024>.
- [23] S.S. Fan, L. Shen, Y. Dong, G. Tian, S.M. Wu, G.G. Chang, C. Janiak, P. Wei, J. S. Wu, X.Y. Yang, sp²-like defect structure of hetero graphene-carbon nanotubes for promoting carrier transfer and stability, *J. Energy Chem.* 57 (2021) 189–197, <https://doi.org/10.1016/j.jechem.2020.09.020>.
- [24] J. Son, S. Lee, S.J. Kim, B.C. Park, H.-K. Lee, S. Kim, J.H. Kim, B.H. Hong, J. Hong, Hydrogenated monolayer graphene with reversible and tunable wide band gap and its field-effect transistor, *Nat. Commun.* 7 (2016) 13261, <https://doi.org/10.1038/ncomms13261>.
- [25] S. Chen, J.J. Duan, J.R. Ran, M. Jaroniec, S.Z. Qiao, N-doped graphene film-confined nickel nanoparticles as a highly efficient three-dimensional oxygen

- evolution electrocatalyst, *Energy Environ. Sci.* 6 (2013) 3693–3699, <https://doi.org/10.1039/C3EE42383B>.
- [26] X. Xu, Y. Li, Y.T. Gong, P.F. Zhang, H.R. Li, Y. Wang, Synthesis of palladium nanoparticles supported on mesoporous N-doped carbon and their catalytic ability for biofuel upgrade, *J. Am. Chem. Soc.* 134 (2012) 16987–16990, <https://doi.org/10.1021/ja308139s>.
- [27] A.K. Singh, S. Jang, J.Y. Kim, S. Sharma, K.C. Basavaraju, M.-G. Kim, K.-R. Kim, J. S. Lee, H.H. Lee, D.-P. Kim, One-pot defunctionalization of lignin-derived compounds by dual-functional $Pd_{50}Ag_{50}/Fe_3O_4/N$ -rGO catalyst, *ACS Catal.* 5 (2015) 6964–6972, <https://doi.org/10.1021/acscatal.5b01319>.
- [28] J.R. Zhang, Y.Q. Chen, F.F. Xu, Y. Zhang, J.Y. Tian, Y. Guo, G.H. Chen, X.Z. Wang, L.J. Yang, Q. Wu, Z. Hu, High-dispersive Pd nanoparticles on hierarchical N-doped carbon nanocages to boost electrochemical CO_2 reduction to formate at low potential, *Small* 19 (2023) e2301577, <https://doi.org/10.1002/smll.202301577>.
- [29] S.Y. Chen, L.Y. Wang, K.C. Chen, C.H. Yeh, W.C. Hsiao, H.Y. Chen, M. Nishi, M. Keller, C.L. Chang, C.N. Liao, T. Mochizuki, H.Y.T. Chen, H.H. Chou, C.M. Yang, Ammonia synthesis over cesium-promoted mesoporous-carbon-supported ruthenium catalysts: Impact of graphitization degree of the carbon support, *Appl. Catal. B-Environ.* 346 (2024) 123725, <https://doi.org/10.1016/j.apcatb.2024.123725>.
- [30] G.M. Liu, Y. Huang, H.Q. Lv, H. Wang, Y.B. Zeng, M.Z. Yuan, Q.G. Meng, C. Y. Wang, Confining single-atom Pd on g-C₃N₄ with carbon vacancies towards enhanced photocatalytic NO conversion, *Appl. Catal. B-Environ.* 284 (2021) 119683, <https://doi.org/10.1016/j.apcatb.2020.119683>.
- [31] D.A. Bulushev, M. Zacharska, E.V. Shlyakhova, A.L. Chuvilin, Y.N. Guo, S. Beloshapkin, A.V. Okotrub, L.G. Bulusheva, Single isolated Pd²⁺ cations supported on N-doped carbon as active sites for hydrogen production from formic acid decomposition, *ACS Catal.* 6 (2015) 681–691, <https://doi.org/10.1021/acscatal.5b02381>.
- [32] C. Jia, M.Y. Pang, Y.D. Lu, Y.Z. Liu, M.H. Zhuang, B.B. Liu, J.H. Lu, T. Wei, L. Wang, T. Bian, M.L. Wang, F.B. Yu, L.M. Sun, L.T. Lin, T. Teng, X. Wu, Z.L. He, J. Gao, J.W. Luo, S.C. Zhang, L. Feng, X.H. Yin, F.Q. You, G. Li, L.X. Zhang, Y.-G. Zhu, X.D. Zhu, Y. Yang, Graphene environmental footprint greatly reduced when derived from biomass waste via flash Joule heating, *One Earth* 5 (2022) 1394–1403, <https://doi.org/10.1016/j.oneear.2022.11.006>.
- [33] C.H. Cui, X.M. Chen, C.J. Liu, Y.N. Zhu, L.Y. Zhu, J.F. Ouyang, Y. Shen, Z.Y. Zhou, F. Qi, In situ reactor-integrated electrospray ionization mass spectrometry for heterogeneous catalytic reactions and its application in the process analysis of high-pressure liquid-phase lignin depolymerization, *Anal. Chem.* 93 (2021) 12987–12994, <https://doi.org/10.1021/acs.analchem.1c02710>.
- [34] H.S. Yu, X.J. Wei, X. Li, S.Q. Gu, S. Zhang, L.H. Wang, J.Y. Ma, L. Li, Q. Gao, Y. Si, The XAFS beamline of SSRF, *Nucl. Sci. Tech.* 26 (2015) 050102, <https://doi.org/10.13538/j.1001-8042/nst.26.050102>.
- [35] L.M. Sun, X. Wu, Y.B. Jiao, C. Jia, T. Teng, L.T. Lin, F.B. Yu, Z.L. He, J. Gao, S. W. Yan, G.S. Shi, R.Z.Y. Jason, J.G. Yang, S.C. Zhang, X.D. Zhu, Millisecond self-heating and quenching synthesis of Fe/carbon nanocomposite for superior reductive remediation, *Appl. Catal. B-Environ.* 342 (2024) 123361, <https://doi.org/10.1016/j.apcatb.2023.123361>.
- [36] J.P. Perdew, K. Burke, M. Ernzerhof, Generalized gradient approximation made simple, *Phys. Rev. Lett.* 77 (1996) 3865, <https://doi.org/10.1103/PhysRevLett.77.3865>.
- [37] D.J. Chadi, Special points for Brillouin-zone integrations, *Phys. Rev. B* 16 (1977) 1746–1747, <https://doi.org/10.1103/PhysRevB.16.1746>.
- [38] H.B. Huang, H.D. Shi, P. Das, J.Q. Qin, Y.G. Li, X. Wang, F. Su, P.C. Wen, S.Y. Li, P. Lu, The chemistry and promising applications of graphene and porous graphene materials, *Adv. Funct. Mater.* 30 (2020) 1909035, <https://doi.org/10.1002/adfm.201909035>.
- [39] M.A.S.R. Saadi, P.A. Advincula, M.S.H. Thakur, A.Z. Khater, S. Saad, A.S. Zeraati, S.K. Nabil, A. Zinke, S. Roy, M.H. Lou, S.N. Bheemasetti, M.A.A. Bari, Y.W. Zheng, J.L. Beckham, V. Gadhamshetty, A. Vashisth, M.G. Kibria, J.M. Tour, P.M. Ajayan, M.M. Rahman, Sustainable valorization of asphaltenes via flash joule heating, *Sci. Adv.* 8 (2022) 1–14, <https://doi.org/10.1126/sciadv.add3555>.
- [40] R. Paul, A. Boruah, R. Das, S. Chakraborty, K. Chahal, D.J. Deka, S.C. Peter, B. K. Mai, J. Mondal, Pyrolysis free out-of-plane Co-single atomic sites in porous organic photopolymer stimulates solar-powered CO_2 fixation, *Small* (2023) 2305307, <https://doi.org/10.1002/smll.202305307>.
- [41] S.G. Wang, P. Zhou, L. Jiang, Z.H. Zhang, K.J. Deng, Y.H. Zhang, Y.X. Zhao, J.L. Li, S. Bottle, H.Y. Zhu, Selective deoxygenation of carbonyl groups at room temperature and atmospheric hydrogen pressure over nitrogen-doped carbon supported Pd catalyst, *J. Catal.* 368 (2018) 207–216, <https://doi.org/10.1016/j.jcat.2018.10.017>.
- [42] C. Pu, J. Zhang, G.G. Chang, Y.Y. Xiao, X.C. Ma, J. Wu, T.T. Luo, K.X. Huang, S. C. Ke, J.X. Li, X.Y. Yang, Nitrogen precursor-mediated construction of N-doped hierarchically porous carbon-supported Pd catalysts with controllable morphology and composition, *Carbon* 159 (2020) 451–460, <https://doi.org/10.1016/j.carbon.2019.12.058>.
- [43] R. Singuru, B. MahipalReddy, K. Dhanalaxmi, J. Mondal, Palladium nanoparticles encaged in a nitrogen-rich porous organic polymer: constructing a promising robust nanoarchitecture for catalytic biofuel upgrading, *ChemCatChem* 9 (2017) 2550–2564, <https://doi.org/10.1002/cctc.201700186>.
- [44] Y.Q. Chen, G.C. Li, Y. Zeng, L.J. Yan, X.Z. Wang, L.J. Yang, Q. Wu, Z. Hu, Boosting faradaic efficiency of CO_2 electroreduction to CO for Fe–N–C single-site catalysts by stabilizing Fe³⁺ sites via F-doping, *Nano Res* 15 (2022) 7896–7902, <https://doi.org/10.1007/s12274-022-4441-0>.
- [45] B. Jiang, X.-G. Zhang, K. Jiang, D.-Y. Wu, W.-B. Cai, Boosting formate production in electrocatalytic CO_2 reduction over wide potential window on Pd surfaces, *J. Am. Chem. Soc.* 140 (2018) 2880–2889, <https://doi.org/10.1021/jacs.7b12506>.
- [46] E. Blanco, D. Carrales-Alvarado, A.B. Dongil, N. Escalona, Effect of the support functionalization of mono- and bimetallic Ni/Co supported on graphene in hydrodeoxygenation of guaiacol, *Ind. Eng. Chem. Res.* 60 (2021) 18870–18879, <https://doi.org/10.1021/acs.iecr.1c03073>.
- [47] Z.P. Chen, W.C. Ren, L.B. Gao, B.L. Liu, S.F. Pei, H.-M. Cheng, Three-dimensional flexible and conductive interconnected graphene networks grown by chemical vapour deposition, *Nat. Mater.* 10 (2011) 424–428, <https://doi.org/10.1038/nmat3001>.
- [48] X.S. Cheng, D.X. Wang, J.C. Liu, X. Kang, H.J. Yan, A.P. Wu, Y. Gu, C.G. Tian, H. G. Fu, Ultra-small Mo₂N on SBA-15 as a highly efficient promoter of low-loading Pd for catalytic hydrogenation, *Nanoscale* 10 (2018) 22348–22356, <https://doi.org/10.1039/C8NR06916F>.
- [49] X.W. Lu, C.M. Guo, M.Y. Zhang, L.P. Leng, J.H. Horton, W. Wu, Z.J. Li, Rational design of palladium single-atoms and clusters supported on silicoaluminophosphate-31 by a photochemical route for chemoselective hydrodeoxygenation of vanillin, *Nano Res* 14 (2021) 4347–4355, <https://doi.org/10.1007/s12274-021-3857-2>.
- [50] P.G. Liu, Z.X. Huang, X.P. Gao, X. Hong, J.F. Zhu, G.M. Wang, Y. Wu, J.A. Zeng, X. S. Zheng, Synergy between palladium single atoms and nanoparticles via hydrogen spillover for enhancing CO_2 photoreduction to CH₄, *Adv. Mater.* 34 (2022) e2200057, <https://doi.org/10.1002/adma.202200057>.
- [51] H.X. Xu, D.J. Cheng, D.P. Cao, X.C. Zeng, A universal principle for a rational design of single-atom electrocatalysts, *Nat. Catal.* 1 (2018) 339–348, <https://doi.org/10.1038/s41929-018-0063-z>.
- [52] L.K. Zhang, N.Z. Shang, S.T. Gao, J.M. Wang, T. Meng, C.C. Du, T.D. Shen, J. Y. Huang, Q.H. Wu, H.J. Wang, Y.Q. Qiao, C. Wang, Y.J. Gao, Z. Wang, Atomically dispersed Co catalyst for efficient hydrodeoxygenation of lignin-derived species and hydrogenation of nitroaromatics, *ACS Catal.* 10 (2020) 8672–8682, <https://doi.org/10.1021/acscatal.0c00239>.
- [53] J. Gao, Y. Cao, G. Luo, J.J. Fan, J.H. Clark, S.C. Zhang, High-efficiency catalytic hydrodeoxygenation of lignin-derived vanillin with nickel-supported metal phosphate catalysts, *Chem. Eng. J.* 448 (2022) 137723, <https://doi.org/10.1016/j.cej.2022.137723>.
- [54] R. Paul, S.C. Shit, T. Fovanna, D. Ferri, B.S. Rao, G.T.K.K. Gunasooriya, D.Q. Dao, Q.V. Le, I. Shown, M.P. Sherburne, Q.T. Trinh, J. Mondal, Realizing catalytic acetophenone hydrodeoxygenation with palladium-equipped porous organic polymers, *ACS Appl. Mater. Interfaces* 12 (2020) 50550–50565, <https://doi.org/10.1021/acsmami.0c16680>.
- [55] W.H. Feng, H.X. Dong, L.B. Niu, X. Wen, L. Huo, G.Y. Bai, A novel $Fe_3O_4@nSiO_2@NiPd-PVP@mSiO_2$ multi-shell core-shell nanocomposite for cinnamic acid hydrogenation in water, *J. Mater. Chem. A* 3 (2015) 19807–19814, <https://doi.org/10.1039/c5ta04894j>.
- [56] Y.N. Zheng, R. Zhang, L. Zhang, Q.F. Gu, Z.-A. Qiao, A resol-assisted cationic coordinative co-assembly approach to mesoporous ABO_3 perovskite oxides with rich oxygen vacancy for enhanced hydrogenation of furfural to furfuryl alcohol, *Angew. Chem. -Int. Ed.* 60 (2021) 4774–4781, <https://doi.org/10.1002/anie.202012416>.